Robust and Automatic Data-Adaptive Beamforming for Multi-Dimensional Arrays

Somasundaram, Samuel; Jakobsson, Andreas; Parsons, Nigel

Published in:
IEEE Transactions on Geoscience and Remote Sensing

DOI:
10.1109/TGRS.2012.2192500

2012

LUND UNIVERSITY

Robust and Automatic Data-Adaptive Beamforming for Multi-Dimensional Arrays

S. D. SOMASUNDARAM, A. JAKOBSSON, AND N. H. PARSONS

Published in: IEEE Trans. Geosci. Remote Sens.
doi:10.1109/TGRS.2012.2192500

Lund 2012

Mathematical Statistics
Centre for Mathematical Sciences
Lund University

Robust and Automatic Data-Adaptive Beamforming for Multi-Dimensional Arrays

S. D. Somasundaram*, *Member, IEEE*, A. Jakobsson†, *Senior Member, IEEE*, and N. H. Parsons*, *Member, IEEE*

***Abstract*— The robust Capon beamformer has been shown to alleviate the problem of signal cancellation resulting from steering vector errors, caused, e.g., by calibration and/or angle-of-arrival errors, which would otherwise seriously deteriorate the performance of an adaptive beamformer. Here, we examine robust Capon beamforming of multi-dimensional arrays, where robustness to angle-of-arrival errors is needed in both azimuth and elevation. It is shown that the commonly used spherical uncertainty sets are unable to control robustness in each of these directions independently. Here, we instead propose the use of flat ellipsoidal sets to control the angle-of-arrival uncertainty. To also allow for other errors, such as calibration errors, we combine these flat ellipsoids with a higher-dimension error ellipsoid. Computationally efficient automatic techniques for estimating the necessary uncertainty sets are derived, and the proposed methods are evaluated using both simulated data and experimental underwater acoustics measurements, clearly showing the benefits of the technique.**

***Index Terms*— Robust beamforming, signal cancellation, ellipsoidal uncertainty sets, underwater acoustics.**

I. Introduction

BEAMFORMING is often used for source localization, power estimation, and for improving the detectability of weak sources (see, e.g., [1]–[3]). As the conventional delay-and-sum (DAS) beamformer is only optimal for a single source embedded in spatially white noise (see, e.g., [4]), the trend has been to employ *adaptive beamforming* techniques, such as the minimum variance distortionless response (MVDR) beamformer (also known as the Capon beamformer) [5], which exploit array covariance measurements to form data-adaptive beams able to achieve superior performance as compared to the DAS beamformer. However, as is well known, the MVDR-type beamformers suffer from the risk of cancellation of the signal-of-interest (SOI) due to array steering vector (ASV) errors and snapshot deficiency [6]–[11]. This makes the issue crucial to consider in any practical system exploiting such beamformers, as, in practice, ASV errors arise naturally as a result of angle-of-arrival (AOA) errors, array calibration errors, and due to deviations from the exploited plane-wave assumptions. The AOA errors are caused by sampling only a coarse grid of angles, often being necessary in practical systems due to, e.g., computational constraints and/or downstream processing requirements, which means that the assumed AOA may be significantly different from the true AOA. Calibration errors arise as a result of sensor gain/phase errors, mutual coupling effects, and/or sensor position errors, whereas deviations from plane-wave assumptions may be caused by near-field sources and/or inhomogeneity of the propagating medium. In order to alleviate these effects, a wealth of *robust adaptive beamforming* techniques have been proposed (see, e.g., [12], [13] and the references therein). Recently, spherical and ellipsoidal uncertainty sets have been exploited to provide robustness to ASV errors [14]–[17]. An appealing property of these techniques is that they maximize the worst-case signal-to-interference-plus-noise ratio (SINR) over the uncertainty set. These approaches, whilst formulated differently, yield equivalent weight vectors; however, the robust Capon beamformer (RCB) algorithms proposed in [16], [17] are the most computationally efficient. In [17], the RCBs were shown to have superior finite sample size performance to the standard Capon beamformer and belong to the class of diagonally loaded beamformers, with the loading level calculated to satisfy the uncertainty set constraints. In general, the performances of the RCBs will depend critically upon the specification of the used uncertainty sets. Most RCB applications have used spherical or flat ellipsoidal sets to beamform uniform linear arrays, where the AOA uncertainty is restricted to a single angle dimension (e.g., azimuth angles), or have used spherical sets to beamform multi-dimensional arrays, where independent restrictions on azimuth and elevation uncertainty were not imposed [16]–[21] (see also [13] and the references therein). In many applications, however, one is interested in beamforming multi-dimensional arrays such that one place restrictions on both the azimuth and elevation AOA uncertainty simultaneously. When spherical uncertainty sets are used, the AOA error can only be controlled in either azimuth or elevation, but not in both. This is a consequence of the fact that the size of a spherical set is described by a single parameter (its radius) and, therefore, cannot be used to independently control azimuth and elevation uncertainty. In this work, we examine alternative approaches to form the necessary uncertainty sets, concluding that flat ellipsoids offer enough flexibility to allow for modeling AOA errors in both azimuth and elevation. In addition to deriving flat ellipsoids via the minimum volume ellipsoid [15], [22], we also examine a computationally simpler low-rank method based on the mean and covariance [23]. However, these flat ellipsoids cannot be used to allow for non-AOA errors, such as calibration errors, covariance estimation errors or those caused

This work was supported in part by the MOD/DTIC, under contract No. RT/COM/4/032, the Swedish Research Council, and Carl Trygger's foundation. Part of this work was presented at the 2009 IEEE Statistical Signal Processing Workshop, Cardiff, U.K.

*S. D. Somasundaram and N. H. Parsons are with the General Sonar Studies Group, Thales Underwater Systems, Dolphin House, Ashurst Drive, Bird Hall Lane, Cheadle Heath, Stockport, Cheshire, SK3 0XB, U.K., email: sdsomasundaram@hotmail.com, nigel.parsons@uk.thalesgroup.com.

†A. Jakobsson is with the Dept. of Mathematical Statistics, Lund University, P.O. Box 118, SE-221 00 Lund, Sweden, email: aj@maths.lth.se.

by wavefront distortion, since these are not accounted for in their design. To overcome this shortcoming, we proceed to extend the proposed flat AOA ellipsoids by combining them with an *error ellipsoid*, to allow for the modeling of non-AOA errors, thereby producing ellipsoids that allow for non-AOA errors as well as for AOA uncertainty in both azimuth and elevation. On both simulated data and data recorded in an underwater acoustics application, we confirm the benefits of using RCBs with these sets. This paper is organized as follows: In the next section, we briefly summarize the RCB approach. In Section III, we discuss the design of ASV uncertainty sets for multi-dimensional arrays. Sections IV and V contain examples on simulated and experimental data, respectively. Finally, Section VI contains our conclusions.

In the following, $(\cdot)^T$, $(\cdot)^H$, $(\cdot)^{-1}$, $(\cdot)^\dagger$, $\mathrm{tr}\{\cdot\}$, $\mathrm{Re}\{\cdot\}$, $\mathrm{Im}\{\cdot\}$, and $\mathrm{E}\{\cdot\}$ denote the transpose, Hermitian transpose, inverse, Moore-Penrose pseudo-inverse, trace, real, imaginary, and expectation operators, respectively. Furthermore, $\sup\{\cdot\}$, $\|\cdot\|_2$ and $\mathrm{diag}\{\mathbf{x}\}$ denote the supremum, the two-norm and a diagonal matrix with the vector $\mathbf{x}$ along the main diagonal. Finally, $\mathbf{X} \geq 0$ is understood to mean that the Hermitian symmetric matrix $\mathbf{X}$ is positive semi-definite.

II. Robust Capon Beamforming

In [16], [17], the RCB was proposed by coupling the covariance fitting formulation of the Capon beamformer [24] with an ellipsoidal uncertainty set, solving

$$\max_{\sigma^2,\mathbf{a}} \sigma^2 \text{ s.t. } \mathbf{R} - \sigma^2 \mathbf{a}\mathbf{a}^H \geq 0, \{\mathbf{a} = \mathbf{B}\mathbf{u} + \bar{\mathbf{a}} \;\big|\; \|\mathbf{u}\|_2 \leq 1\} \quad (1)$$

with $\mathbf{R} \in \mathbb{C}^{M\times M}$, σ^2 and $\mathbf{a} \in \mathbb{C}^{M\times 1}$ denoting the array covariance matrix, the SOI power and its ASV, respectively, and where M denotes the number of array elements. The assumed actual array steering vector is thus viewed as allowing the assumed steering vector, $\bar{\mathbf{a}}$, to vary within the given uncertainty ellipsoid. The center of the ellipsoid is defined by $\bar{\mathbf{a}}$, and its principal semi-axes by the unit-norm left singular vectors of the (full column rank) matrix $\mathbf{B} \in \mathbb{C}^{M\times L}$, scaled by the corresponding singular values.

A. Non-Degenerate and Spherical Uncertainty Sets

If $\mathbf{B}$ in (1) is square, such that $L = M$, the set is termed non-degenerate (ND), and one may write $\mathbf{a} \;\big|\; [\mathbf{a}-\bar{\mathbf{a}}]^H \mathbf{C}^{-1} [\mathbf{a}-\bar{\mathbf{a}}] \leq 1$, where $\mathbf{C} = \mathbf{B}\mathbf{B}^H$. Then, (1) reduces to [16], [17]

$$\min_{\mathbf{a}} \mathbf{a}^H \mathbf{R}^{-1} \mathbf{a} \quad \text{s.t.} \quad (\mathbf{a} - \bar{\mathbf{a}})^H \mathbf{C}^{-1} (\mathbf{a} - \bar{\mathbf{a}}) \leq 1. \quad (2)$$

To exclude the trivial solution $\mathbf{a} = \mathbf{0}$, it is assumed that $\bar{\mathbf{a}}^H \mathbf{C}^{-1} \bar{\mathbf{a}} > 1$. Letting

$$\mathbf{C}^{-1} = \frac{1}{\epsilon} \mathbf{D}^H \mathbf{D} \quad (3)$$

and forming $\breve{\mathbf{a}} = \mathbf{D}\mathbf{a}$, $\breve{\bar{\mathbf{a}}} = \mathbf{D}\bar{\mathbf{a}}$ and $\breve{\mathbf{R}} = \mathbf{D}\mathbf{R}\mathbf{D}^H$, (2) can be rewritten as

$$\min_{\breve{\mathbf{a}}} \breve{\mathbf{a}}^H \breve{\mathbf{R}}^{-1} \breve{\mathbf{a}} \quad \text{s.t.} \quad \left\|\breve{\mathbf{a}} - \breve{\bar{\mathbf{a}}}\right\|_2^2 \leq \epsilon, \quad (4)$$

where the constraint is now a spherical one. Denoting $\hat{\breve{\mathbf{a}}}$ as the solution[1] to (4), an estimate of the ASV is formed as

$$\hat{\mathbf{a}}_0 = \mathbf{D}^{-1} \hat{\breve{\mathbf{a}}}. \quad (5)$$

Setting $\mathbf{B} = \sqrt{\epsilon}\mathbf{I}$, yields a spherical set with radius $\sqrt{\epsilon}$.

B. Flat Uncertainty Set

When $\mathbf{B}$ is rectangular, so that $L < M$, the ellipsoid is termed flat or degenerate, and (1) reduces to [17]

$$\min_{\mathbf{u}} (\mathbf{B}\mathbf{u} + \bar{\mathbf{a}})^H \mathbf{R}^{-1} (\mathbf{B}\mathbf{u} + \bar{\mathbf{a}}) \quad \text{s.t.} \quad \|\mathbf{u}\|_2 \leq 1. \quad (6)$$

To exclude the trivial solution $\mathbf{a} = \mathbf{0}$, it is assumed that $\bar{\mathbf{a}}^H \left(\mathbf{B}^\dagger\right)^H \mathbf{B}^\dagger \bar{\mathbf{a}} > 1$. Denoting $\hat{\mathbf{u}}$ as the solution[1] to (6), an estimate of the ASV is formed as

$$\hat{\mathbf{a}}_0 = \mathbf{B}\hat{\mathbf{u}} + \bar{\mathbf{a}}. \quad (7)$$

Given the estimate $\hat{\mathbf{a}}_0$ from either (5) or (7), the ASV is scaled so that its Euclidean length squared equals M, forming

$$\hat{\hat{\mathbf{a}}}_0 = \left(\sqrt{M}\hat{\mathbf{a}}_0\right) / \|\hat{\mathbf{a}}_0\|_2 . \quad (8)$$

Then, the RCB power and weight estimates are given by $\hat{\sigma}_0^2 = \frac{1}{\hat{\mathbf{a}}_0^H \mathbf{R}^{-1} \hat{\mathbf{a}}_0}$ and $\mathbf{w} = \frac{\mathbf{R}^{-1}\hat{\mathbf{a}}_0}{\hat{\mathbf{a}}_0^H \mathbf{R}^{-1} \hat{\mathbf{a}}_0}$. We remark that in the RCB optimization in (1), the norm of the ASV is not constrained, but is scaled later, as in (8). In [18] and [25], doubly constrained RCBs (DCRCBs) were derived assuming that the ASV lies within the uncertainty set and has a constant norm. Here, we do not examine the DCRCBs, but remark that they could exploit the ellipsoids derived herein.

III. Array Steering Vector Uncertainty Sets

In this section, we present methods to form spherical, flat, and ND (ellipsoidal) ASV uncertainty sets, for a single beam that is parameterized by an azimuth and elevation angle pair and their respective angle uncertainties. For wide-band applications, it is assumed that the time-series data are Fourier transformed to a suitable resolution and that these sets are estimated for each frequency bin, though for notational convenience we do not include the frequency parameter in the following exposition. We remark that by estimating sets for each frequency bin, one can obtain constant power-width beamformers (see, e.g., [19]). Initially, we discuss the estimation of sets allowing for AOA uncertainty, and then, where needed, proceed to extend these to allow for other forms of uncertainty. Let θ and ϕ denote a generic center point for the range of considered azimuth and elevation angles, respectively, thus indicating the center for the region of interest for these angles. These center points can be determined by possible *a priori* information of the region of interest, for instance due to the look angle of the system. In many practical systems, the azimuth/elevation space is sampled using a fixed number of beams. Then, the beamformer used for a given beam is not being designed to pass an SOI at a single azimuth/elevation angle pair (θ, ϕ), but is expected to pass an SOI whose azimuth and elevation angle may be anywhere with a range of values.

[1] We refer the reader to [16], [17] for solutions to (4) and (6).

Without loss of generality, let Δ_{Az} and Δ_{El} denote the allowed deviations for a beam with center points, θ and ϕ, such that the AOA is allowed to vary within the azimuth and elevation ranges

$$\Theta_{\text{Az}} = [\theta - 0.5\Delta_{\text{Az}}, \theta + 0.5\Delta_{\text{Az}}] \quad (9)$$

$$\Phi_{\text{El}} = [\phi - 0.5\Delta_{\text{El}}, \phi + 0.5\Delta_{\text{El}}] \quad (10)$$

respectively, thus forming a rectangle in azimuth/elevation angle space.The dual-directional array steering vector is evaluated over $N_{\text{Az}}N_{\text{El}}$ uniformly distributed sampling points, forming a set

$$\mathcal{A} = \left\{\mathbf{a}(\theta_k, \phi_l)\right\}_{k,l} \; k = 1, \ldots, N_{\text{Az}}, \; l = 1, \ldots, N_{\text{El}}, \quad (11)$$

where $\mathbf{a}(\theta_k, \phi_l)$ is calculated from the delays of a plane-wave impinging on the array from direction azimuth θ_k and elevation ϕ_l (see, e.g., [4], [12]), where

$$\theta_k = \theta + \left(\frac{k-1}{N_{\text{Az}}-1} - \frac{1}{2}\right)\Delta_{\text{Az}} \quad (12)$$

$$\phi_l = \phi + \left(\frac{l-1}{N_{\text{El}}-1} - \frac{1}{2}\right)\Delta_{\text{El}}. \quad (13)$$

Using the above definitions, we proceed to discuss the estimation of different types of uncertainty sets.

A. Spherical Uncertainty Sets

Spherical uncertainty sets are a common choice in the literature. The (squared) radius of the uncertainty sphere, ϵ, can be selected as $\epsilon \geq \|\mathbf{a} - \bar{\mathbf{a}}\|_2^2$, $\forall\ \mathbf{a} \in \mathcal{A}$. Here, to handle AOA errors and to guarantee that all the ASVs simulated over the ROI belong to the sphere, one may select $\epsilon = \epsilon_{\text{sph}}$, where

$$\epsilon_{\text{sph}} = \sup_{k,l} \|\mathbf{a}(\theta_k, \phi_l) - \bar{\mathbf{a}}\|_2^2, \quad (14)$$

for $k = [1, \ldots, N_{\text{Az}}]$, $l = [1, \ldots, N_{\text{El}}]$, and where θ_k and ϕ_l are given by (12) and (13), respectively. Often the sphere center is selected as

$$\bar{\mathbf{a}} = \mathbf{a}(\theta, \phi), \quad (15)$$

which is the ASV at the middle of the ROI, usually termed the assumed ASV [17], [21]. Alternatively, one could choose $\bar{\mathbf{a}}$ as the mean of the ASVs covering the ROI, that is as

$$\bar{\mathbf{a}} = \frac{1}{N_{\text{Az}}N_{\text{El}}} \sum_{k=1}^{N_{\text{Az}}} \sum_{l=1}^{N_{\text{El}}} \mathbf{a}(\theta_k, \phi_l). \quad (16)$$

In [13] (Ch. 3), a tighter spherical set was proposed, based on the observation that $\mathbf{R} - \sigma^2\mathbf{a}\mathbf{a}^H$ is unchanged by a phase shift of $\mathbf{a}$. Specifically, ϵ is chosen so that

$$\epsilon \geq \min_{\alpha} \left\|\mathbf{a}e^{i\alpha} - \bar{\mathbf{a}}\right\|_2^2 \quad \forall \mathbf{a} \in \mathcal{A}. \quad (17)$$

It was noted in [13] that such an approach will not affect the SOI power estimate or the output SNR, but can produce phase errors in signal waveform estimates. Using this approach to allow for AOA uncertainty, we may choose $\epsilon = \epsilon_{\text{tight}}$, where

$$\begin{aligned} \epsilon_{\text{tight}} &= \sup_{k,l} \min_{\alpha} \left\|\mathbf{a}(\theta_k, \phi_l)e^{i\alpha} - \bar{\mathbf{a}}\right\|_2^2 \\ &= \sup_{k,l} \left\| \mathbf{a}(\theta_k, \phi_l) \left(\frac{\mathbf{a}(\theta_k, \phi_l)^H \bar{\mathbf{a}}}{\bar{\mathbf{a}}^H \mathbf{a}(\theta_k, \phi_l)}\right)^{1/2} - \bar{\mathbf{a}} \right\|_2^2 \end{aligned} \quad (18)$$

for $k = 1, \ldots, N_{\text{Az}}$ and $l = 1, \ldots, N_{\text{El}}$. In the following, the sets denoted "Spherical Middle" and "Spherical Mean" have centers formed from (15) and (16), respectively, and radii calculated using (14). The sets denoted "Tight Spherical Middle" and "Tight Spherical Mean" have centers formed from (15) and (16), respectively, and radii calculated using (18). To summarize, the following steps are required

1) For a given beam with a ROI defined by, e.g. (9) and (10), form the set of $N_{\text{Az}}N_{\text{El}}$ complex vectors $\mathcal{A}$ in (11).
2) For "Spherical Middle" or "Tight Spherical Middle", form the set center using (15). For "Spherical Mean" or "Tight Spherical Mean", form the set center using (16).
3) For "Spherical Middle" or "Spherical Mean", use (14) to calculate the set radius. For "Tight Spherical Middle" or "Tight Spherical Mean", use (18) to calculate the set radius.

Since the spherical uncertainty set size is described by a single parameter, its radius, it is clear that it cannot be used to restrict elevation and azimuth AOA uncertainty independently. This aspect is discussed further in Section IV. Here, the sets have been designed to allow for AOA error only, however, since spherical sets allow for arbitrary norm bounded errors, they are often robust to a whole host of other error types.

B. Flat Ellipsoidal Uncertainty Sets

As spherical sets are unable to control AOA uncertainty independently in both azimuth and elevation, we proceed to examine alternative sets. Since real ellipsoids can generally be formed tighter than their complex counterparts [15], [23], we transform to the real space $\mathbb{R}^{2M}$, forming the set $\mathcal{Z}$ from $\mathcal{A}$, using the element $\mathbf{z} = \left[\ \text{Re}\left\{\mathbf{a}^T\right\} \quad \text{Im}\left\{\mathbf{a}^T\right\}\ \right]^T$ in $\mathcal{Z}$ from each element $\mathbf{a} \in \mathcal{A}$. One alternative is to estimate the minimum volume ellipsoid (MVE), containing the points in $\mathcal{Z}$ [15], [23]. We also consider an approach based upon the estimation of the mean and covariance of the elements in $\mathcal{Z}$, which we term the low-rank (LR) method.

1) Minimum Volume Ellipsoid Method: Here, we briefly describe the procedure, proposed in [15], for computing the MVE covering the $N_{\text{Az}}N_{\text{El}}$ points in $\mathcal{Z}$, which for notational convenience we here index as $\{\mathbf{z}_k\}_{k=1}^{N_{\text{Az}}N_{\text{El}}}$. Assuming that the points used to estimate the MVE are m-dimensional, we remark that procedures for computing the MVE require that the affine hull of these points must span $\mathbb{R}^m$ [13], [22]. Consequently, if we were to apply such procedures directly to the set of points in $\mathcal{Z}$, we would require that their affine hull spanned $\mathbb{R}^{2M}$. As seen in [23], this is often not the case and the (real versions of the) ASVs sampling the ROI will often not span all of $\mathbb{R}^{2M}$, but will lie in a subspace of lower dimension, say L. We therefore apply a rank-preserving affine transformation, $f(\mathbf{z}) = \mathbf{U}_1^T(\mathbf{z} - \mathbf{z}_1)$, to each member of $\mathcal{Z}$, where $\mathbf{U}_1$ consists of the L dominant left singular vectors of the following $2M \times (N_{\text{Az}}N_{\text{El}} - 1)$ matrix

$$\left[\ (\mathbf{z}_2 - \mathbf{z}_1) \quad (\mathbf{z}_3 - \mathbf{z}_1) \quad \ldots \quad (\mathbf{z}_{N_{\text{Az}}N_{\text{El}}} - \mathbf{z}_1)\ \right]. \quad (19)$$

This results in a new set of $N_{\text{Az}}N_{\text{El}}$ samples lying in $\mathbb{R}^L$, which we denote $\tilde{\mathcal{Z}}$ and contains the points $\{\tilde{\mathbf{z}}_k\}_{k=1}^{N_{\text{Az}}N_{\text{El}}}$. The non-degenerate MVE in $\mathbb{R}^L$, described by $\{\tilde{\mathbf{B}}\mathbf{u} + \tilde{\bar{\mathbf{a}}} | \ \|\mathbf{u}\|_2 \leq 1\}$,

is then found by solving

$$\min_{\mathbf{M},\mathbf{g}} \; -\ln\det\mathbf{M} \quad \text{subject to} \tag{20}$$
$$\left(\mathbf{M}\tilde{\mathbf{z}}_k - \mathbf{g}\right)^T \left(\mathbf{M}\tilde{\mathbf{z}}_k - \mathbf{g}\right) \leq 1, \quad \mathbf{M} > 0$$

for $k = 1, \ldots, N_{\text{Az}}N_{\text{El}}$, where $\tilde{\mathbf{B}} = \mathbf{M}^{-1}$ and $\tilde{\bar{\mathbf{a}}} = \mathbf{M}^{-1}\mathbf{g}$. The flat MVE in $\mathbb{R}^{2M}$ is described by $\{\mathbf{B}\mathbf{u} + \bar{\mathbf{a}} \,|\, \|\mathbf{u}\|_2 \leq 1\}$, where $\mathbf{B} = \mathbf{U}_1\tilde{\mathbf{B}}$ and $\bar{\mathbf{a}} = \mathbf{U}_1\tilde{\bar{\mathbf{a}}} + \mathbf{z}_1$. Evaluating (20) is computationally intensive, quickly becoming intractable as $N_{\text{Az}}N_{\text{El}}$ and/or L become large. A theoretical complexity bound on computing the MVE from m points was given in [26] as $\mathcal{O}(m^{3.5}\ln[m/\eta)])$ operations to a relative accuracy of η in the volume. For further details on solving (20), we refer the reader to the computationally efficient, combined interior-point and active set method proposed in [22].

2) Low-rank Method: An alternative, computationally cheaper method, is to treat the points in $\mathcal{Z}$ as random vectors and compute the ellipsoid from their mean and covariance. A similar approach was used for one-dimensional arrays in [15]. For a multidimensional array, we compute $\bar{\mathbf{a}}$ and $\mathbf{C}$ as

$$\bar{\mathbf{a}} = \frac{1}{N_{\text{Az}}N_{\text{El}}} \sum_{k=1}^{N_{\text{Az}}} \sum_{l=1}^{N_{\text{El}}} \mathbf{z}(\theta_k, \phi_l) \tag{21}$$

$$\mathbf{C} = \frac{1}{\beta}\mathbf{C}', \tag{22}$$

where θ_k and ϕ_l are given by (12) and (13), and where

$$\mathbf{C}' = \frac{1}{N_{\text{Az}}N_{\text{El}}} \sum_{k=1}^{N_{\text{Az}}} \sum_{l=1}^{N_{\text{El}}} \left[\mathbf{z}(\theta_k, \phi_l) - \bar{\mathbf{a}}\right]\left[\mathbf{z}(\theta_k, \phi_l) - \bar{\mathbf{a}}\right]^H \tag{23}$$

with $\mathbf{z}(\theta_k, \phi_l) = \left[\begin{array}{cc} \text{Re}\left\{\mathbf{a}^T(\theta_k, \phi_l)\right\} & \text{Im}\left\{\mathbf{a}^T(\theta_k, \phi_l)\right\} \end{array}\right]^T$, and where

$$\beta = \sup_{k,l} \left[\mathbf{z}(\theta_k, \phi_l) - \bar{\mathbf{a}}\right]^H \mathbf{C}'^{-1} \left[\mathbf{z}(\theta_k, \phi_l) - \bar{\mathbf{a}}\right], \tag{24}$$

for $k = [1, \ldots, N_{\text{Az}}]$ and $l = [1, \ldots, N_{\text{El}}]$. The scaling by β is required to ensure that all of the points used to estimate the ellipsoid also belong to the resulting ellipsoid. That is, so that $\left[\mathbf{z}(\theta_k, \phi_l) - \bar{\mathbf{a}}\right]^H \mathbf{C}^{-1} \left[\mathbf{z}(\theta_k, \phi_l) - \bar{\mathbf{a}}\right] \leq 1$, for $k = [1, \ldots, N_{\text{Az}}]$ and $l = [1, \ldots, N_{\text{El}}]$. As shown in [15], providing that the inverse exists, the ellipsoid may be formed with center $\bar{\mathbf{a}}$ as given in (21) and configuration matrix $\mathbf{B} = \mathbf{C}^{1/2}$, where $\mathbf{C}$ is given by (22). Often, however, the estimate $\mathbf{C}'$ in (23) is rank-deficient, indicating that the AOA uncertainty ellipsoid is flat. We remark that such a scenario was not considered in [15]. In this case, the calculation of β in (24) is not possible as $\mathbf{C}'^{-1}$ will not exist. Furthermore, a rank-deficient $\mathbf{C}$ cannot be used in the RCB with the ND ellipsoidal uncertainty proposed in [16], [17], since $\mathbf{C}^{-1}$ in (3) will not exist. In the following, we therefore propose a method for calculating a flat ellipsoid from $\mathbf{C}'$ by, firstly, factorizing $\mathbf{C}'$ using the singular value decomposition (SVD) as $\mathbf{C}' = \mathbf{U}_{\mathbf{C}}\mathbf{\Lambda}_{\mathbf{C}}\mathbf{V}_{\mathbf{C}}^H$, where $\mathbf{U}_{\mathbf{C}}$ and $\mathbf{V}_{\mathbf{C}}$ contain the left and right singular vectors, respectively, and where $\mathbf{\Lambda}_{\mathbf{C}} = \text{diag}\left\{\left[\begin{array}{ccc} \lambda_1 & \ldots & \lambda_{2M} \end{array}\right]\right\}$ contains the singular values $\lambda_1 \geq \ldots \geq \lambda_{2M}$ arranged in non-increasing order on the main diagonal. The best rank-L approximation of $\mathbf{C}'$ is given by the truncated SVD (see, e.g., [27]) $\mathbf{C}'_L = \mathbf{U}_{\mathbf{C},L}\mathbf{\Lambda}_{\mathbf{C},L}\mathbf{V}_{\mathbf{C},L}^H$, where $\mathbf{U}_{\mathbf{C},L}$, $\mathbf{V}_{\mathbf{C},L}$, and $\mathbf{\Lambda}_{\mathbf{C},L}$ are formed using the L dominant singular vectors and values. Clearly, as $\mathbf{C}'$ is guaranteed to be symmetric positive semi-definite, $\mathbf{U}_{\mathbf{C}} = \mathbf{V}_{\mathbf{C}}$ and $\mathbf{\Lambda}_{\mathbf{C}}$ will only contain real non-negative values. Let

$$\mathbf{B}' = \mathbf{U}_{\mathbf{C},L}\mathbf{\Lambda}_{\mathbf{C},L}^{1/2}, \tag{25}$$

where $\mathbf{C}'_L = \mathbf{B}'\mathbf{B}'^H$. To ensure that the $N_{\text{Az}}N_{\text{El}}$ points in $\mathcal{Z}$ lie within the ellipsoid, we form

$$\mathbf{B} = \beta'\mathbf{B}', \tag{26}$$

where

$$\beta' = \sup_{k,l} \left\|\mathbf{B}'^{\dagger}(\mathbf{z}(\theta_k, \phi_l) - \bar{\mathbf{a}})\right\|_2, \tag{27}$$

for $k = [1, \ldots, N_{\text{Az}}]$ and $l = [1, \ldots, N_{\text{El}}]$. We term this the low-rank (LR) method for computing the AOA uncertainty ellipsoid, whose main computational burden is forming the SVD of $\mathbf{C}'$. Whilst ellipsoids derived via the mean and covariance are not as tight as those derived via the MVE [15], [23], their computation is simpler. Further, as we shall see in Sections IV and V, in both cases the ellipsoids typically need altering to allow for other errors such as calibration errors.

3) Dimension Selection: An important practical consideration is how to choose the dimension of the LR or MV ellipsoids, something not considered in most of the earlier works. In [23], the dimension of the ellipsoids were chosen via mean-squared error (MSE) plots of the power, requiring prior evaluation of the ellipsoids and manual scanning of the MSE plots. Such an approach is prohibitive in practice, since sets often need to be estimated for multiple frequency bins, azimuth angles and elevation angles. We note that in [23], the LR and MVE MSE results were similar, indicating that their optimal dimensions are probably similar. Thus, a dimension selection method working well for one method would likely work well for the other. Here, we propose an automatic method that does not require prior evaluation of the ellipsoids and is based upon the SVD of $\mathbf{C}'$ in (23), which is required for evaluating the LR ellipsoid. The singular values of $\mathbf{C}'$ represent the distribution of the $N_{\text{Az}}N_{\text{El}}$ samples of the array response among each of the left singular vectors, where the left singular vectors represent a basis for the AOA uncertainty. Therefore, one may choose the dimension such that the energy in the basis is greater than or equal to a fraction of the total energy. Specifically, we choose L as the smallest integer such that

$$\frac{\sum_{l=1}^{L}\lambda_l}{\text{tr}\{\mathbf{C}'\}} > \gamma, \tag{28}$$

where $0 < \gamma < 1$ represents the minimum fraction of the total energy contained in the associated basis. Clearly, the smaller γ, the greater the reduction in robustness to AOA uncertainty; however, choosing it larger will increase the rank of $\mathbf{B}$, increasing the computational load of the flat RCB, and also decreasing the gain against noise. We will discuss the effect of varying γ further in Section IV. We remark that combining this dimension selection method with the LR method, results in a fast automatic method of estimating flat ellipsoids providing robustness to AOA uncertainty, since the SVD of $\mathbf{C}'$ is exploited in both methods. To summarize, the

following steps are required to compute the parameters $\mathbf{B}$ and $\bar{\mathbf{a}}$ defining a "Flat LR" ellipsoid or a "Flat MVE", exploiting our dimension selection rule.

1) For a given beam with a ROI defined by, e.g. (9) and (10), form the set of $N_{\text{Az}}N_{\text{El}}$ complex vectors $\mathcal{A}$ in (11) and then form the set of real vectors $\mathcal{Z}$ from $\mathcal{A}$.
2) Form $\bar{\mathbf{a}}$ using (21) and $\mathbf{C}'$ using (23).
3) Calculate the SVD, $\mathbf{C}' = \mathbf{U}_{\mathbf{C}}\mathbf{\Lambda}_{\mathbf{C}}\mathbf{V}_{\mathbf{C}}^H$.
4) Given γ and the singular values of $\mathbf{C}'$, calculate the flat ellipsoid dimension L using (28).
5) For the "Flat LR " set: (a) form $\mathbf{U}_{\mathbf{C},L} \in \mathbb{C}^{M\times L}$ and $\mathbf{\Lambda}_{\mathbf{C},L} \in \mathbb{C}^{L\times L}$ from the dominant left singular vectors and values, (b) form $\mathbf{B}'$ using (25) and β' using (27), (c) the ellipsoid is formed from $\mathbf{B} = \beta'\mathbf{B}'$ with center given by (21), calculated above in step 2. For "Flat MVE": (a) Calculate $\mathbf{U}_1$ as the L dominant singular vectors of (19), (b) Apply $f(\mathbf{z}) = \mathbf{U}_1^T(\mathbf{z} - \mathbf{z}_1)$ to the points in $\mathcal{Z}$, to form the set $\tilde{\mathcal{Z}}$, (c) use techniques in, e.g., [22], to solve (20) for $\mathbf{M}$ and $\mathbf{g}$, (d) the "Flat MVE" is defined by $\mathbf{B} = \mathbf{U}_1\mathbf{M}^{-1}$ and center $\bar{\mathbf{a}} = \mathbf{B}\mathbf{g} + \mathbf{z}_1$.

C. Non-Degenerate Ellipsoidal Uncertainty Sets

So far, the discussion has not allowed for the possibility of non-AOA errors, such as calibration errors or those caused by wave-front distortion. We now proceed to examine also such errors, assuming that these can be well modeled as additive errors (to the ASV) and are described by an *error ellipsoid*, $\mathcal{E}(\mathbf{a}_{\text{err}}, \mathbf{B}_{\text{err}})$. We note that in [15], calibration errors were assumed multiplicative and were propagated via the outer approximation to the Hadamard product. Assuming that the ellipsoids describing the AOA errors and the non-AOA errors are given by $\mathcal{E}(\bar{\mathbf{a}}, \mathbf{B}) = \left\{\mathbf{B}\mathbf{u} + \bar{\mathbf{a}} \middle| \|\mathbf{u}\|_2 \le 1\right\}$ and $\mathcal{E}(\mathbf{a}_{\text{err}}, \mathbf{B}_{\text{err}}) = \left\{\mathbf{B}_{\text{err}}\mathbf{u} + \mathbf{a}_{\text{err}} \middle| \|\mathbf{u}\|_2 \le 1\right\}$, respectively, one may use the results in [15], [28] to write their sum as

$$\mathcal{E}\left(\check{\mathbf{a}}, \check{\mathbf{C}}(p)^{1/2}\right) = \left\{\check{\mathbf{C}}(p)^{1/2}\mathbf{u} + \check{\mathbf{a}} \middle| \|\mathbf{u}\|_2 \le 1\right\}, \tag{29}$$

with

$$\check{\mathbf{a}} = \bar{\mathbf{a}} + \mathbf{a}_{\text{err}} \tag{30}$$

$$\check{\mathbf{C}}(p) = (1 + p^{-1})\mathbf{B}\mathbf{B}^T + (1 + p)\mathbf{B}_{\text{err}}\mathbf{B}_{\text{err}}^T, \tag{31}$$

and where p is often chosen to minimize either the determinant or trace of $\check{\mathbf{C}}(p)$, or to produce the MVE. However, minimizing the determinant requires $\mathcal{O}(M^3)$ operations and is ill-posed for degenerate ellipsoids, whilst calculating the MVE requires the solution to a generalized eigenvalue problem, also requiring $\mathcal{O}(M^3)$ operations. Thus, both these methods would likely be excluded from online updating of the sum of the ellipsoids. Minimizing the trace is the most computationally efficient of these approaches, requiring only $\mathcal{O}(M)$ operations, and its solution can be written in closed form as

$$\hat{p} = \sqrt{\frac{\text{tr}(\mathbf{B}\mathbf{B}^T)}{\text{tr}(\mathbf{B}_{\text{err}}\mathbf{B}_{\text{err}}^T)}}. \tag{32}$$

In the following, the sets "ND Trace LR" and "ND Trace MVE" denote sets, formed from "Flat LR" sets and "Flat MVE" sets, respectively, and by using the trace combination method, which uses (30) as the set center, and (32) in (31).

It is possible to form a computationally simpler solution than the trace-based method that also has better source localization results. This is done by replacing (31) with

$$\check{\mathbf{C}} = \mathbf{B}\mathbf{B}^T + \mathbf{B}_{\text{err}}\mathbf{B}_{\text{err}}^T, \tag{33}$$

which is similar to adding the covariances describing the two ellipsoids (where the ellipsoid center is still given by (30)). Sets obtained via (33) are denoted ND[2] sets. In the following, "ND LR" and "ND MVE" denote ND sets obtained from "Flat LR" and "Flat MVE" sets, respectively.

In many applications, calibration data is scarce and information on the statistics of the wave-front distortion errors non-existent; consequently, a special case of interest is using a conservative, spherical error ellipsoid with radius $\sqrt{\check{\epsilon}}$, i.e., setting $\mathbf{a}_{\text{err}} = \mathbf{0}$ and $\mathbf{B}_{\text{err}} = \sqrt{\check{\epsilon}}\mathbf{I}$. Then, $\check{\mathbf{C}} = \mathbf{B}\mathbf{B}^T + \check{\epsilon}\mathbf{I}$, whose inverse, for general $\mathbf{B}$, can be written as

$$\check{\mathbf{C}}^{-1} = \frac{1}{\check{\epsilon}}\mathbf{I} - \frac{1}{\check{\epsilon}^2}\mathbf{B}\left(\mathbf{I} + \frac{1}{\check{\epsilon}}\mathbf{B}^T\mathbf{B}\right)^{-1}\mathbf{B}^T, \tag{34}$$

which needs only $\mathcal{O}(L^3)$, instead of $\mathcal{O}(M^3)$, operations. We exploit (34) when computing the proposed "ND MVE" set for $\mathbf{B}_{\text{err}} = \sqrt{\check{\epsilon}}\mathbf{I}$. Further computational savings can be made if $\mathbf{B}$ is computed via the LR method, for which one may write $\check{\mathbf{C}}$ as in (35), given at the top of next page. We note that the RCB in [17] exploits the matrix $\check{\mathbf{D}}$ and its inverse, where $\check{\mathbf{C}}^{-1} = \check{\mathbf{D}}^H\check{\mathbf{D}}$ [see (3)–(5)], where one may thus form

$$\check{\mathbf{D}} = \check{\mathbf{\Gamma}}^{-\frac{1}{2}}\mathbf{U}_{\mathbf{C}}^H, \tag{36}$$

with $\check{\mathbf{\Gamma}}^{-\frac{1}{2}}$ defined as in (37), given at the top of next page. In some situations, it might be useful to adjust the value of $\check{\epsilon}$, e.g., to reduce the size of the uncertainty set and trade good power estimation performance for possibly better detection performance and/or spatial resolution. An important advantage of the proposed "ND LR" approach is that the update of $\check{\mathbf{D}}$ (and its inverse), as a result of an update of $\check{\epsilon}$, can be done computationally efficiently using (36) and (37), as no numerical matrix inversion is required.

We summarize the steps required to produce the aforementioned sets, given a flat AOA ellipsoid defined by $\mathbf{B}$ with center $\bar{\mathbf{a}}$ and an error ellipsoid defined by $\mathbf{B}_{\text{err}}$ with center $\mathbf{a}_{\text{err}}$.

1) Form the ellipsoid center $\check{\mathbf{a}}$ using (30).
2) For "ND Trace LR" or "ND Trace MVE": (a) form $\hat{p}$ using (32), (b) form $\check{\mathbf{C}}(\hat{p})$ using (31) with $\hat{p}$. The set is then $\mathbf{a}|[\mathbf{a} - \check{\mathbf{a}}]^H\check{\mathbf{C}}(\hat{p})^{-1}[\mathbf{a} - \check{\mathbf{a}}]$, where generally $\check{\mathbf{C}}(\hat{p})^{-1}$ and its associated square root (see (3)) are computed numerically[3].
   For "ND MVE" or "ND LR" with general $\mathbf{B}_{\text{err}}$, form $\check{\mathbf{C}}$ using (33). The set is then $\mathbf{a}|[\mathbf{a} - \check{\mathbf{a}}]^H\check{\mathbf{C}}^{-1}[\mathbf{a} - \check{\mathbf{a}}]$ where also $\check{\mathbf{C}}^{-1}$ and its associated square root are computed numerically.

[2]Generally, combining the AOA and *error* ellipsoids may not produce a ND ellipsoid, though in practice, where one needs to allow for calibration and/or covariance matrix errors, the resulting set will likely be ND. Thus, for notational simplicity, we term the set ND.

[3]We remark that when $\mathbf{B}_{\text{err}} = \sqrt{\check{\epsilon}}\mathbf{I}$, the "ND Trace MVE" and "ND Trace LR" sets could be computed more efficiently using equations analogous to (34) and (36), respectively. However, as they have poorer properties than the "ND LR" and "ND MVE" sets, we have omitted these here.

$$\check{\mathbf{C}} = \mathbf{B}\mathbf{B}^T + \check{\epsilon}\mathbf{I} = \left[\begin{array}{cc} \mathbf{U}_{\mathbf{C},L} & \mathbf{U}_{\mathbf{C},M-L} \end{array} \right] \left[\begin{array}{cc} |\beta'|^2\mathbf{\Lambda}_{\mathbf{C},L} + \check{\epsilon}\mathbf{I}_L & 0 \\ 0 & \check{\epsilon}\mathbf{I}_{M-L} \end{array} \right] \left[\begin{array}{c} \mathbf{U}_{\mathbf{C},L}^H \\ \mathbf{U}_{\mathbf{C},M-L}^H \end{array} \right] \triangleq \mathbf{U}_{\mathbf{C}}\check{\mathbf{\Gamma}}\mathbf{U}_{\mathbf{C}}^H \tag{35}$$

$$\check{\mathbf{\Gamma}}^{-\frac{1}{2}} = \text{diag}\left\{ \left[\begin{array}{ccccccc} \frac{1}{(|\beta'|^2\lambda_1+\check{\epsilon})^{1/2}} & \cdots & \frac{1}{(|\beta'|^2\lambda_L+\check{\epsilon})^{1/2}} & \frac{1}{\check{\epsilon}^{1/2}} & \cdots & \frac{1}{\check{\epsilon}^{1/2}} \end{array} \right] \right\} \tag{37}$$

For "ND MVE" with $\mathbf{B}_{\text{err}} = \sqrt{\check{\epsilon}}\mathbf{I}$, compute $\check{\mathbf{C}}^{-1}$ using (34). The associated square root is computed numerically. For "ND LR" with $\mathbf{B}_{\text{err}} = \sqrt{\check{\epsilon}}\mathbf{I}$, write the square root $\check{\mathbf{D}}$ using (36), (37) and $\mathbf{U}_{\mathbf{C}}$. Note that $\check{\mathbf{D}}^{-1}$ can be written as $\check{\mathbf{D}}^{-1} = \mathbf{U}_{\mathbf{C}}\check{\mathbf{\Gamma}}^{\frac{1}{2}}$.

In Section IV, when using "ND LR" with $\mathbf{B}_{\text{err}} = \sqrt{\check{\epsilon}}\mathbf{I}$, we find that if γ is set too large when estimating the flat LR AOA ellipsoid, so that the AOA uncertainty is overfitted, the loss in control of AOA uncertainty is greater for the same value of $\check{\epsilon}$. The reason for this is that when the AOA ellipsoid is overfitted, the smallest dominant eigenvalues of $\mathbf{C}'$ in (23) are very small and so will give a very small weighting to the associated eigenvectors when used to calculate $\mathbf{B}'$ in (25). However, as shown in (35), when a spherical error ellipsoid is added, the contributions of these eigenvectors is significantly increased due to the weighting by $\check{\epsilon}$. The trace-based method significantly compromises AOA uncertainty, especially so for larger values of γ. For ND Trace LR, the reasons for this can be understood as follows: For the special case of a spherical error ellipsoid, (32) can be written as

$$\hat{p} = \sqrt{\frac{|\beta'|^2 \sum_{k=1}^{L} \lambda_k}{M\check{\epsilon}}}. \tag{38}$$

Also, one may write $\check{\mathbf{C}}(p) = \mathbf{U}_{\mathbf{C}}\check{\mathbf{\Gamma}}_p\mathbf{U}_{\mathbf{C}}^H$, where

$$\check{\mathbf{\Gamma}}_p = \left[\begin{array}{cc} (1+\hat{p}^{-1})|\beta'|^2\mathbf{\Lambda}_{\mathbf{C},L} + (1+\hat{p})\check{\epsilon}\mathbf{I}_L & \mathbf{0} \\ \mathbf{0} & (1+\hat{p})\check{\epsilon}\mathbf{I}_{M-L} \end{array} \right]$$

Numerical simulations show that, for practical values of $\boldsymbol{\gamma}$, the $|\beta'|^2\lambda_k$, for $k = 1, \ldots, L$, are relatively large compared to $\check{\epsilon}$. In such cases, (38) imply that $\hat{p}$ will be greater (often significantly) than unity, therefore enhancing the spherical uncertainty and suppressing the control of AOA uncertainty.

IV. Simulated Data Examples

Here, we examine simulated data examples using a planar array, consisting of two rows of ten sensors, with half-wavelength spacing. In the following, we select a region of interest (ROI), where a source may be present, as the region covering azimuth and elevation angles in the ranges $\bar{\Theta}_{\text{Az}} = [-117.5, -112.5]$ and $\bar{\Phi}_{\text{El}} = [105, 115]$ degrees, respectively, and design the uncertainty sets to cover this region. Therefore, in (9) and (10), we set $\theta = -115°$, $\Delta_{\text{Az}} = 5°$, $\phi = 110°$, and $\Delta_{\text{El}} = 10°$. We evaluate the performance of the RCB for the ten different types of uncertainty set, "Spherical Middle", "Spherical Mean", "Tight Spherical Middle", "Tight Spherical Mean", "Flat LR", "Flat MVE", "ND Trace LR", "ND Trace MVE", "ND LR" and "ND MVE". We assume a spherical error ellipsoid in the latter four sets.

A. Localization Patterns

Here, we evaluate how well the different sets are able to protect against SOI cancellation for a source lying inside the ROI, but still provide good rejection of a source that is outside of the ROI. To do this, we simulate a single source, corrupted by white Gaussian noise, at varying azimuth and elevation angles, in steps of 0.5 degrees, over the intervals $[-135, -95]$ and $[70, 150]$, respectively. At each azimuth/elevation angle pair (θ_s, ϕ_s), the beamformers are provided with the theoretical covariance matrix, given by $\mathbf{R}(\theta_s, \phi_s) = \sigma_s^2\mathbf{a}(\theta_s, \phi_s)\mathbf{a}(\theta_s, \phi_s)^H + \mathbf{I}$, where $\mathbf{a}(\theta_s, \phi_s)$ and σ_s^2 denote the source ASV and its power. In the following, we set $\sigma_s^2 = 60$ dB. At each azimuth/elevation angle pair, the beamformer weights and power are estimated. Though the source position, adaptive weights and beamformer power estimate can change at each new angle, the uncertainty set is fixed as the one designed to cover the ROI. We term the resulting plot a localization pattern[4]. For good robustness to AOA uncertainty, the beamformer should not suppress the source when it is inside the ROI. However, for good localization, it should also suppress the source when it is outside of the ROI. For an ideal beamformer, one would thus desire the beamformer power estimate to be zero outside the ROI, whereas the power of the source is undistorted within it. Figures 1(a), (b), (c) and (d) show the localization patterns for "Spherical Middle" with $\epsilon_{\text{sph}} = 10.2$, "Tight Spherical Middle", with $\epsilon_{\text{tight}} = 4.3$, "Spherical Mean" with $\epsilon_{\text{sph}} = 8.8$ and "Tight Spherical Mean" with $\epsilon_{\text{tight}} = 4.0$, respectively, indicating that they all provide robustness to AOA uncertainty, but the tight spherical sets gives better suppression of the source when it lies outside of the ROI, as compared to the spherical sets. That is, the tight spherical sets give better localization of a source than the spherical sets. There does not appear to be any significant difference in the localization pattern between selecting the sphere center as the ASV at the middle of the ROI, or selecting it as the mean of the ASVs covering the ROI. From Figures 1(a)-(d), we see that in order to control the azimuth uncertainty, the radii of the spheres are too large to control the elevation uncertainty. This is a result of the fact that, for our array, the horizontal aperture is greater than the vertical aperture and, therefore, the rate of change of phase (of the ASV elements) with azimuth angle is greater than

[4]We remark that these patterns are different from both beampatterns and power patterns. To produce a beampattern, one plots $\left|\mathbf{w}^H\mathbf{a}(\theta, \phi)\right|^2$ for different values of θ and ϕ, but fixed $\mathbf{w}$. Our pattern is different because we do not fix $\mathbf{w}$. In a power pattern, one fixes $\mathbf{a}$ in a direction and plots $\left|\mathbf{w}^H(\theta, \phi)\mathbf{a}\right|^2$, recalculating $\mathbf{w}(\theta, \phi)$ for different values of θ and ϕ. Our pattern is different because we do not fix $\mathbf{a}$.

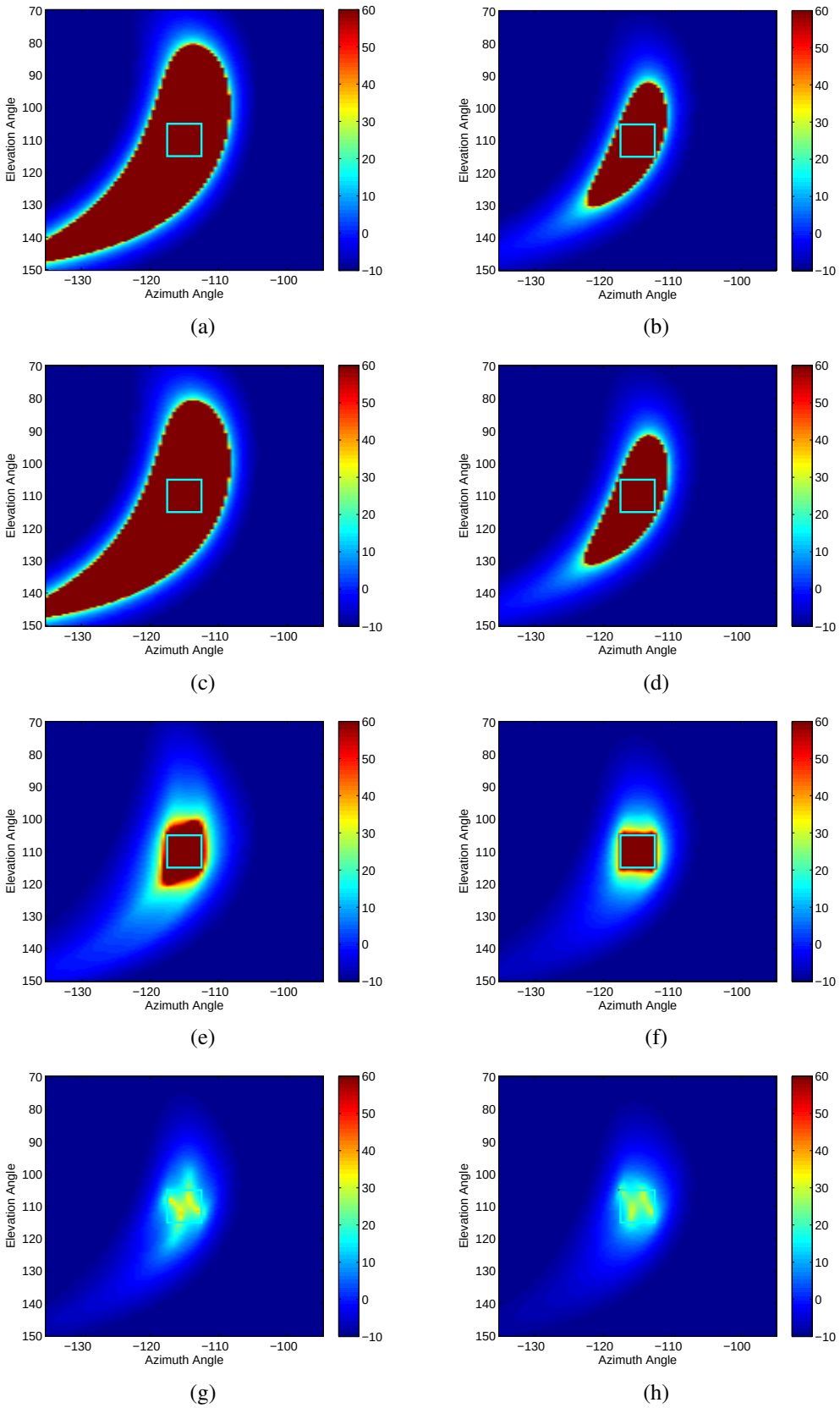

Fig. 1. For a ROI shown by the square, when there is no calibration uncertainty, the localization patterns for (a) Spherical Middle, (b) Tight Spherical Middle, (c) Spherical Mean, (d) Tight Spherical Mean, (e) Flat LR with $1-\gamma=-80$ dB, (f) Flat MVE with $1-\gamma=-80$ dB, (g) Flat LR with $1-\gamma=-20$ dB and (h) Flat MVE with $1-\gamma=-20$ dB.

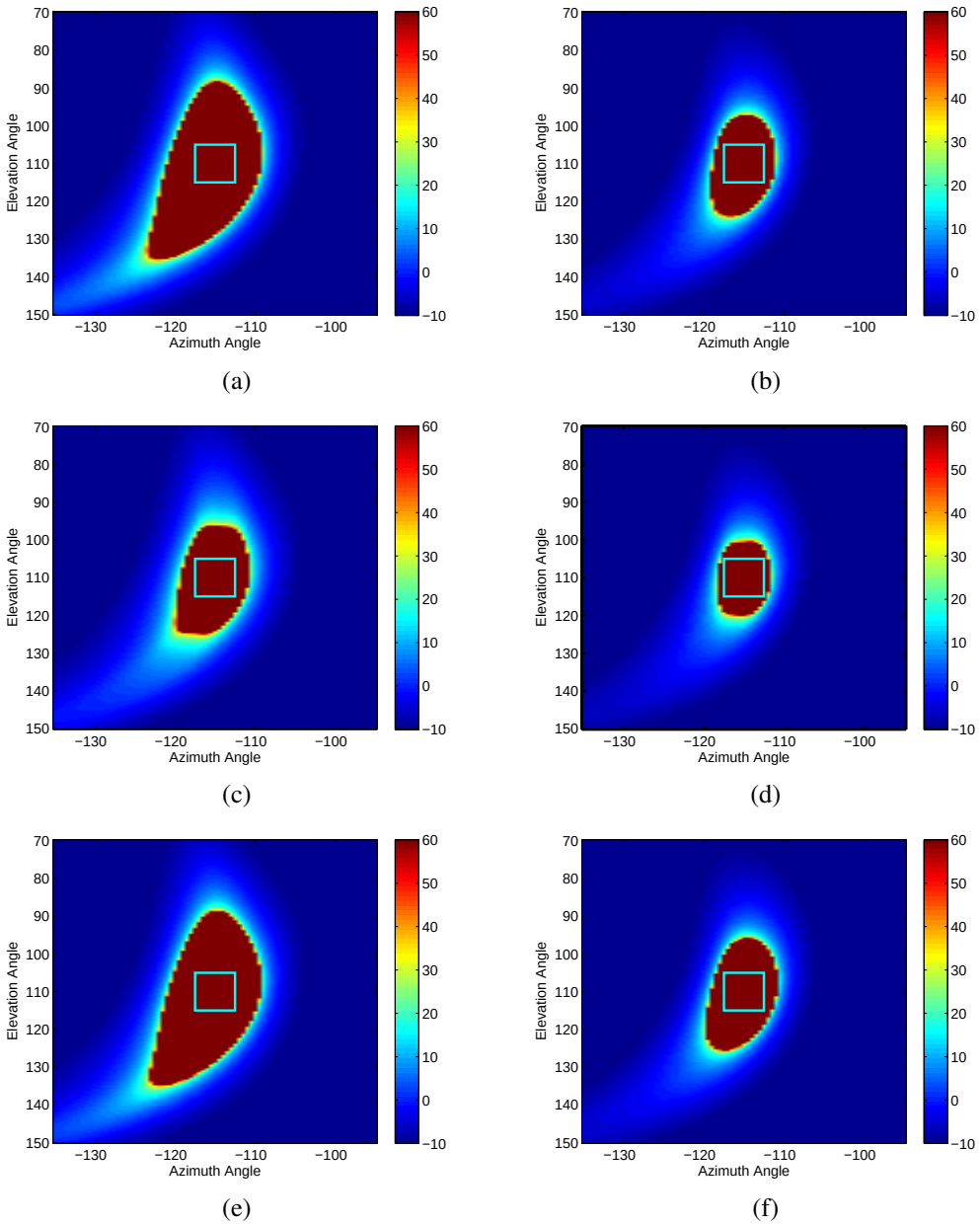

Fig. 2. Localization patterns, when $1-\gamma=-80$ dB for (a) ND Trace LR with $\breve{\epsilon}=0.1$, (b) ND Trace MVE with $\breve{\epsilon}=0.1$, (c) ND LR with $\breve{\epsilon}=0.1$, (d) ND MVE with $\breve{\epsilon}=0.1$, (e) ND LR with $\breve{\epsilon}=1$ and (f) ND MVE with $\breve{\epsilon}=1$.

that for elevation angle. Therefore, to control an x-degree error in azimuth, a larger value of ϵ is required than to control an x-degree error in elevation. For $1-\gamma=-80$ dB, Figures 1(e) and 1(f) illustrate the localization patterns of the flat LR and MV ellipsoidal sets, respectively, and show that, unlike the spherical sets, these are able to provide much tighter control of AOA uncertainty in both elevation and azimuth, as they give much better rejection of the source, when it lies outside of the ROI. As expected, the MVE allows for a tighter control of AOA uncertainty than the LR ellipsoid. We remark that for $1-\gamma=-80$ dB, the dimension of the LR and MV ellipsoids was selected as $L=11$ using (28). Figures 1(g) and 1(h) show the same results, but with $1-\gamma=-20$ dB, which gives $L=3$, illustrating that SOI cancellation can occur with a flat uncertainty set even if there is only AOA error, if γ is not chosen large enough. For $1-\gamma=-80$ dB, Figure 2 shows localization patterns for the ND sets. Comparing the patterns in Figure 2 with Figures 1(e) and 1(f), it is clear that including a spherical error ellipsoid with the flat ellipsoids reduces the ability to reject a source that is close to, but outside of the ROI. Figures 2(a)–(d) show results for the four different ND sets for $\breve{\epsilon}=0.1$, illustrating that, as discussed in Section III-C, the ND sets obtained by using the trace method have much poorer localization properties than their counterparts, obtained by the proposed combination method. Thus, we now only examine localization patterns for ND sets derived using our proposed method which uses (33). Comparing Figures 2(e) and (f) with (c) and (d), shows that the larger the error sphere radius is in ND LR and ND MVE, the further away the source has to be from the ROI before it is treated as

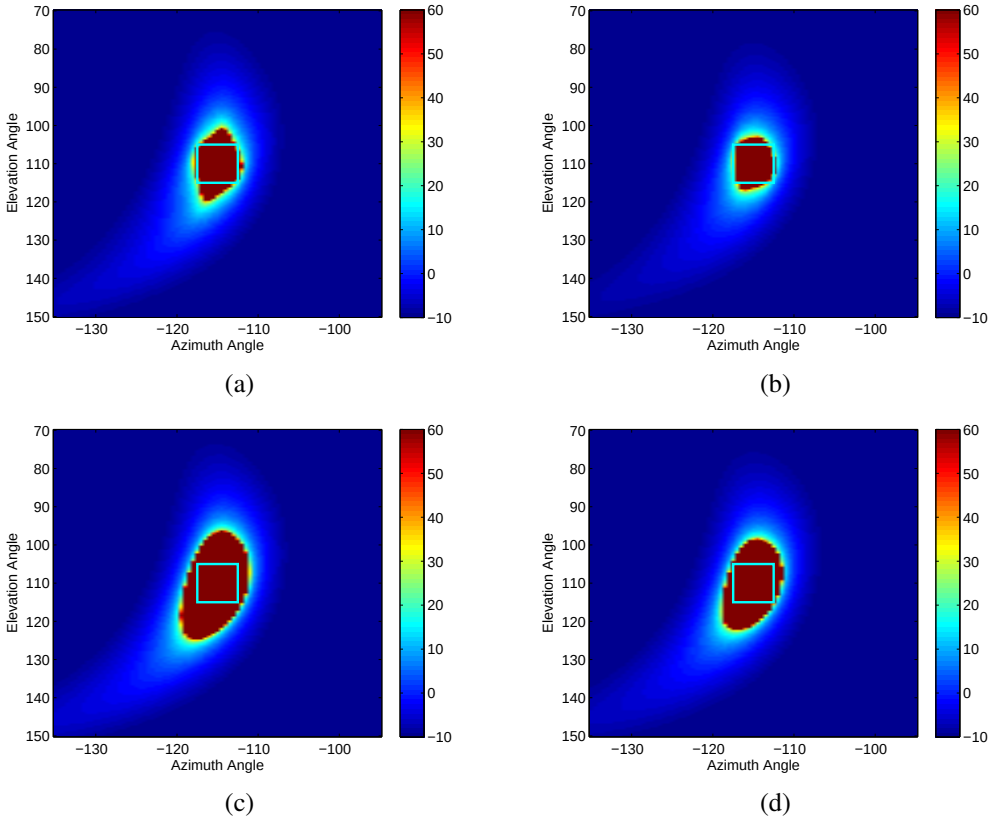

Fig. 3. Localization patterns, when $1-\gamma=-20$ dB, for (a) ND LR with $\check{\epsilon}=0.1$, (b) ND MVE with $\check{\epsilon}=0.1$, (c) ND LR with $\check{\epsilon}=1$, and (d) ND MVE with $\check{\epsilon}=1$.

an interference and rejected. We remark that increasing the error sphere radius in the ND Trace sets also has this effect. Figures 3(a)–(d) show the same patterns as in Figures 2(c)–(f), but now with sets derived using a smaller value of γ, such that $1-\gamma=-20$ dB. We remark that the SOI cancellation exhibited by the original flat ellipsoids, whose localization patterns are shown in Figures 1(g) and 1(h), has been mitigated by combining them with a spherical error ellipsoid. Further, note that for same value of $\check{\epsilon}$, increasing γ increases the region where a source will not be rejected. This observation could be important, e.g., if we knew that the calibration errors were large, so that a large value of $\check{\epsilon}$ was needed, we might want to reduce the value of γ (thereby, reducing the dimension of the used flat ellipsoid) in order to ensure a good rejection of sources outside of the ROI. Figure 4 illustrates results when the source ASV has been simulated with calibration errors. Specifically, the previous source ASV $\mathbf{a}(\theta_s,\phi_s)$, at angle pair (θ_s,ϕ_s), is now replaced with $\mathbf{s}(\theta_s,\phi_s)=\mathbf{a}(\theta_s,\phi_s)+\mathbf{e}$, where $\mathbf{e}$ is a complex circularly symmetric random vector, such that $\|\mathbf{e}\|_2^2=\sigma_e^2$. Comparing Figures 4(a) and 4(b) with Figures 1(a) and 1(b), it is clear that the spherical and tight spherical uncertainty sets are robust to the addition of these arbitrary errors, as a source within the ROI is not canceled. We remark that similar results are obtained for the Spherical Mean and Tight Spherical Mean sets. However, comparing Figures 4(c) and 4(d) with Figures 1(e) and 1(f), indicates that the flat ellipsoids are not robust to these arbitrary errors. Comparing Figures 4(e) and (f) with Figures 2 (c) and (d), it is clear that the proposed ND sets are also robust to these arbitrary errors. We remark that the ND Trace sets are also robust to calibration errors. So far, we have seen that flat ellipsoids are very good for controlling AOA uncertainty in both elevation and azimuth, but they are not robust to arbitrary errors such as calibration errors that are typically encountered in practice. The spherical uncertainty sets are good at allowing for all types of error, though have poor control of AOA uncertainty. By combining the flat ellipsoids with a spherical error ellipsoid, we are able to make the flat uncertainty sets robust against arbitrary errors, yielding sets with good robustness to both AOA and non-AOA uncertainty, and also with good localization properties.

B. Interference Rejection Properties

A key beamforming criterion is the signal-to-interference-plus-noise ratio (SINR), defined as $\text{SINR}=\frac{\sigma_0^2}{\sigma_n^2}\frac{\left|\mathbf{w}^H\mathbf{a}_0\right|^2}{\mathbf{w}^H\mathbf{Q}\mathbf{w}}$, where $\mathbf{w}$, σ_0^2, $\mathbf{a}_0$, σ_n^2 and $\mathbf{Q}$ denote the weight vector, the SOI power, the SOI ASV, the noise-plus-interference power and the noise-plus-interference covariance matrix, which is normalized such that $\text{tr}(\mathbf{Q})=M$. The input, receiver, signal-to-noise ratio (SNR) is given by $\text{SNR}=\frac{\sigma_0^2}{\sigma_n^2}$. In the following, the data covariance is given by $\mathbf{R}=\sigma_0^2\mathbf{a}_0\mathbf{a}_0^H+\mathbf{Q}$, where the noise-plus-interference covariance is given by $\mathbf{Q}=\sum_{k=1}^{d}\sigma_k^2\mathbf{a}_k\mathbf{a}_k^H+\sigma_w^2\mathbf{I}$, which consists of terms due to d zero-mean uncorrelated interfering sources, where for the kth interferer, σ_k^2 and $\mathbf{a}_k$ denote the source power and ASV, and a white noise term $\sigma_w^2\mathbf{I}$, with power σ_w^2. From the localization patterns, it is clear that

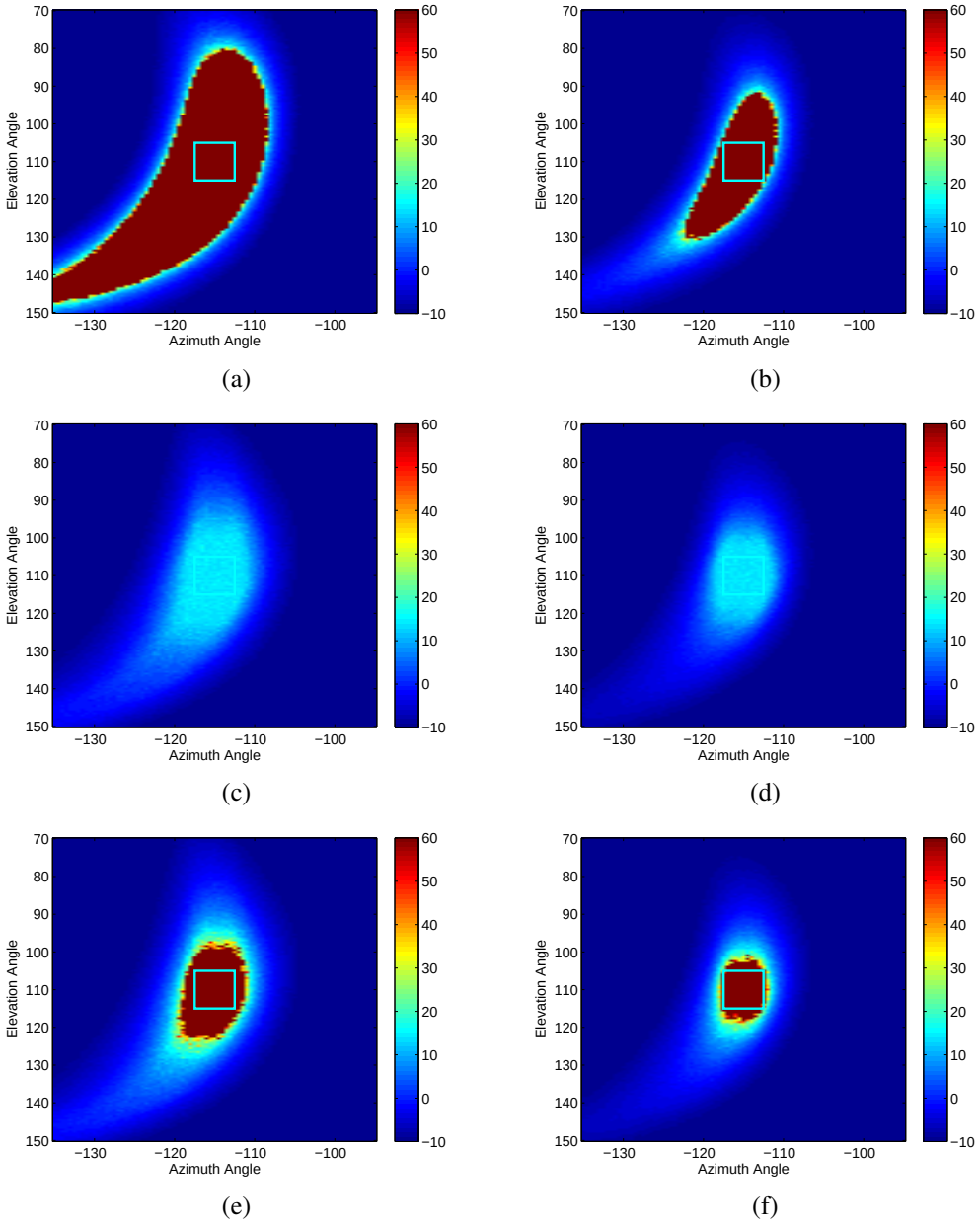

Fig. 4. For a ROI shown by the square, when there is calibration uncertainty such that $\sigma_e^2 = 0.05$, the localization patterns for (a) Spherical Middle, (b) Tight Spherical Middle, (c) Flat LR with $1-\gamma = -80$ dB, (d) Flat MVE with $1-\gamma = -80$ dB, and when using $1-\gamma = -80$ dB and $\check{\epsilon} = 0.1$, (e) ND LR and (f) ND MVE.

the main differences between algorithms using the different sets will be rejecting interferers close to the ROI. Thus, we examine how well the different algorithms are able to reject interferers that lie close to the ROI, but not inside of it. At each Monte-Carlo simulation, we simulate the SOI, anywhere within the ROI, and a set of d discrete interferers, whose locations are random but are anywhere within $\pm 5^\circ$ in azimuth and $\pm 20^\circ$ in elevation from the ROI center, but not in the ROI. We set $\sigma_w^2 = 0$ dB, and $\sigma_k^2 = 40$ dB for $k = 1, \ldots, d$. Using the sets estimated above, and where applicable with $1-\gamma = -80$ dB and $\check{\epsilon} = 0.1$, Figures 5(a) and 5(b) illustrate SINR versus SNR, for $d = 3$, when there is or is not calibration error. For the low SNR, interference and noise limited case, there is a clear gain over the spherical sets for all of the flat and ND sets, apart from the ND Trace LR set. This gain is due to the sets being able to null interferers that lie close to the ROI. In the case of the ND Trace LR set, it behaves similarly to a spherical uncertainty set as the trace combination method has emphasized the spherical error ellipsoid. As the SNR is increased, the flat ellipsoids perform well providing there is no arbitrary error. For low SNRs the tight spherical sets outperform the spherical sets as they are able to reject interference that lies closer to the ROI. Figures 5(c) and 5(d) show the same plots, except now γ has been reduced so that $1-\gamma = -20$ dB. Now, the SINR for the flat uncertainty sets is compromised at high SNR, even when there is no calibration error. This loss in SINR is mitigated, however, if the flat set is combined with a spherical error ellipsoid. Note that the

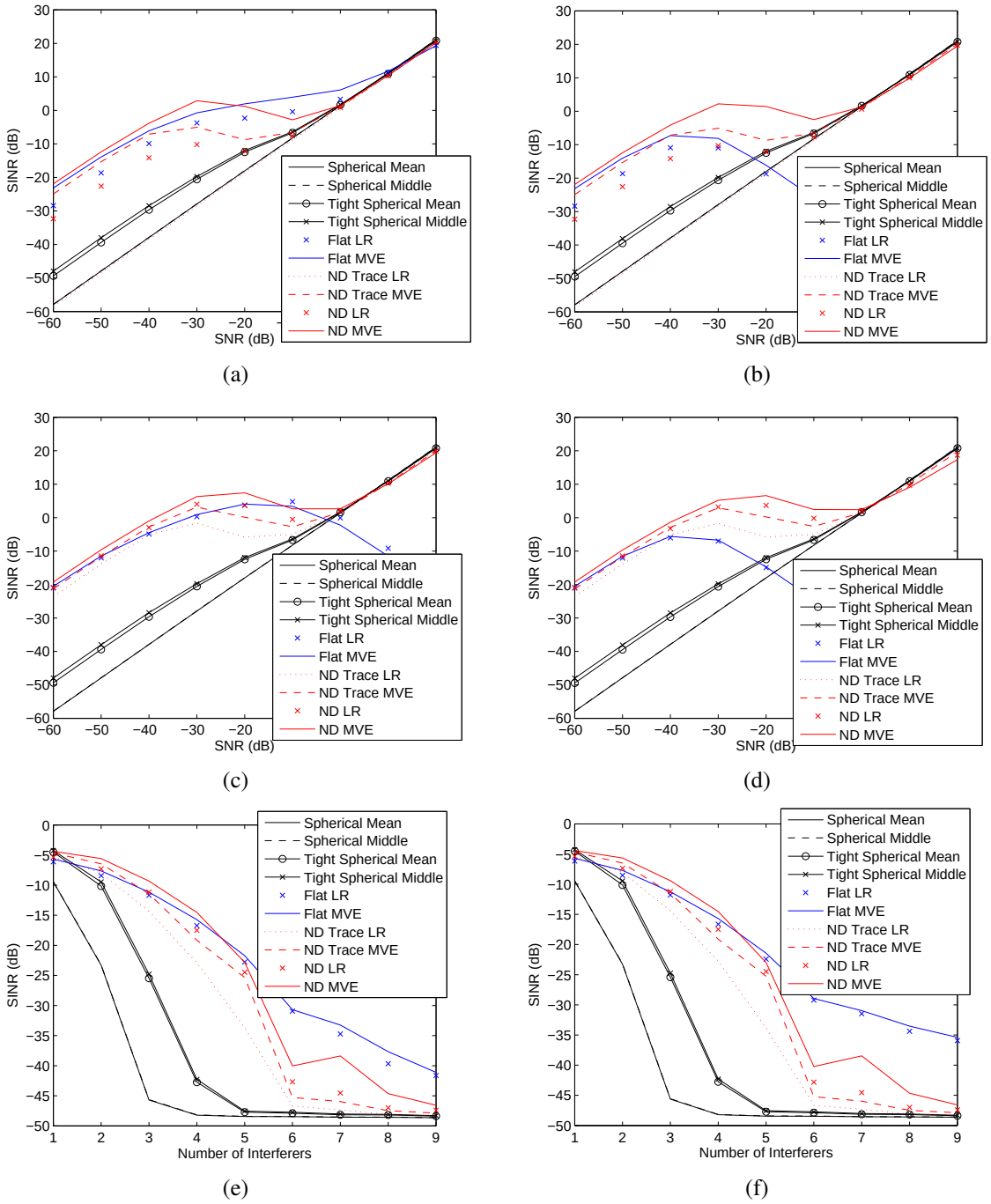

Fig. 5. For MC = 500, SINR vs SNR for three 40 dB interferers within $\pm 5^\circ$ in azimuth and $\pm 20^\circ$ in elevation of ROI center when (a) $\sigma_e^2 = 0$ and $1-\gamma = -80$ dB, (b) $\sigma_e^2 = 0.05$ and $1-\gamma = -80$ dB, (c) $\sigma_e^2 = 0$ and $1-\gamma = -20$ dB, (d) $\sigma_e^2 = 0.05$ and $1-\gamma = -20$ dB, and for SNR = -50dB, SINR vs d for (e) $1-\gamma = -20$ dB and $\sigma_e^2 = 0$, and (f) $1-\gamma = -20$ dB with $\sigma_e^2 = 0.05$.

performance when using a ND set constructed from a flat LR ellipsoid is greatly improved by selecting γ lower. The ND sets constructed using a flat MVE appear less sensitive to the choice of γ. Figures 5(e) and 5(f) show SINR as a function of the number of interferers for an interference and noise limited situation, when there is or is not calibration error. Again, we observe that significant gains are achievable if using either flat or ND sets. Figures 6(a) and 6(b) illustrate the SINR versus the radius of the error ellipsoid for an interference and noise limited situation and a high SNR situation, respectively. In the low SNR, interference and noise limited situation, the smaller the error ellipsoid, the higher the SINR. This is because we wish to shrink the uncertainty set size to not allow in noise and interference. Further, for low SNR, SOI cancellation due to ASV errors is less problematic. However, for a high SNR situation, increasing the size of the error ellipsoid in order to allow for the calibration errors is important to prevent SOI cancellation. These results highlight why one would like to be able to update the ND sets online as a function of the error sphere radius, $\sqrt{\check{\epsilon}}$. Note also then that as $\check{\epsilon}$ is decreased,

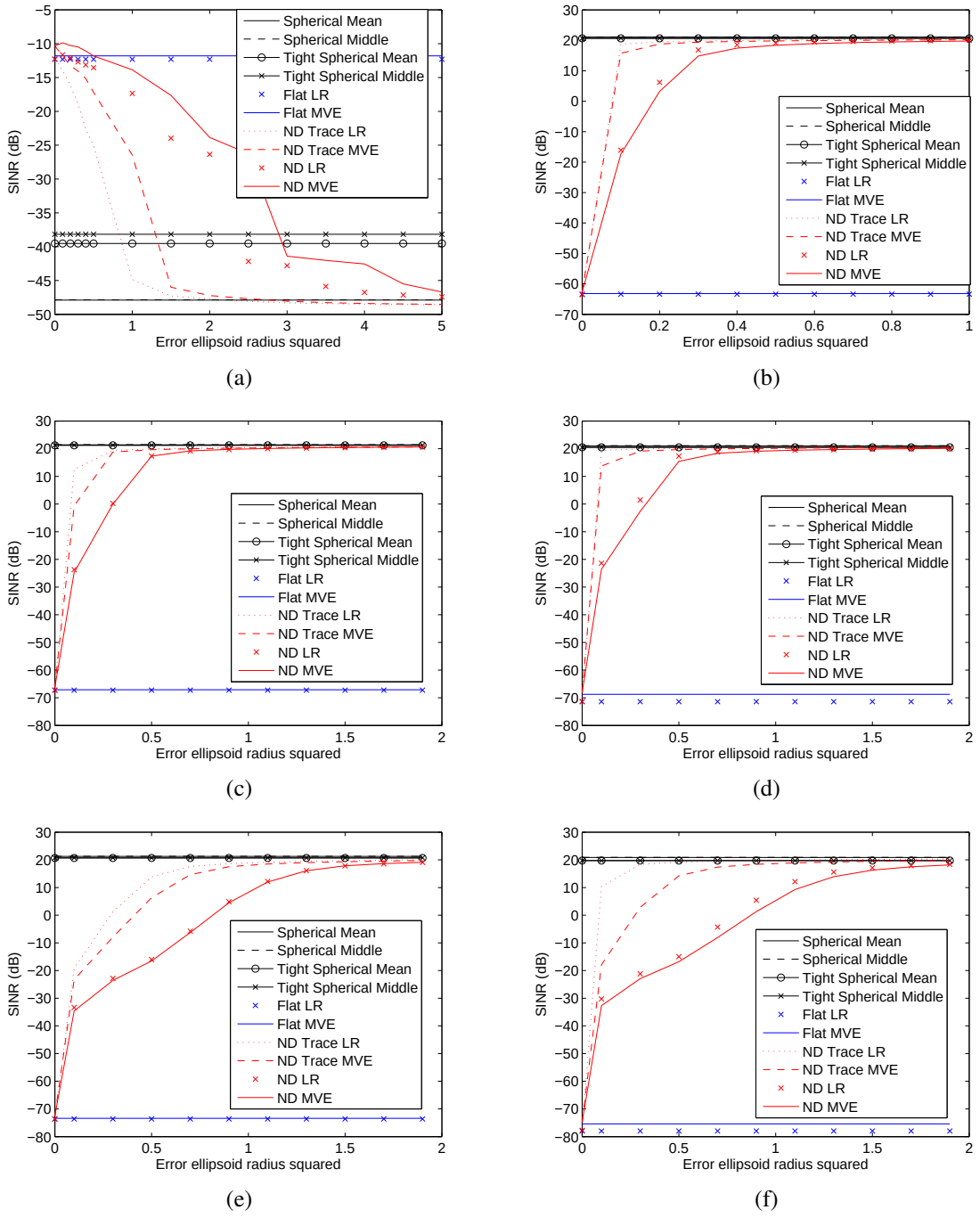

Fig. 6. For MC = 500 and for three 40 dB interferers within $\pm 5^\circ$ in azimuth and $\pm 20^\circ$ in elevation of ROI center, SINR vs $\check{\epsilon}$ when (a) SNR = -50 dB, $\sigma_e^2 = 0.25$ and $1-\gamma = -20$ dB, (b) SNR = 20 dB, $\sigma_e^2 = 0.25$ and $1-\gamma = -20$ dB, and for SNR = 20 dB, (c) $\sigma_e^2 = 0.5$ and $1-\gamma = -20$ dB, (d) $\sigma_e^2 = 0.5$ and $1-\gamma = -80$ dB, (e) $\sigma_e^2 = 1.5$ and $1-\gamma = -20$ dB and (f) $\sigma_e^2 = 1.5$ and $1-\gamma = -80$ dB.

the performance of a ND set tends to the associated flat set, whilst increasing the radius of the error sphere means performance tends to a spherical uncertainty set. Figures 6(c)-(f) illustrate SINR versus $\check{\epsilon}$ plots for different values of σ_e^2 and γ, illustrating that, for ND LR and ND MVE, there is no significant differences for the different values of γ, and that there is a clear correlation between the value of σ_e^2 and the value of $\check{\epsilon}$ at which they converge to the (tight) spherical set SINR. It appears that in ND LR and ND MVE one should select $\check{\epsilon}$ at least as large as σ_e^2. The ND Trace LR and ND Trace MVE algorithms converge at much lower value of $\check{\epsilon}$ and are more sensitive to the choice of γ.

V. Experimental Data Examples

Here, we examine results on data measured using a planar underwater acoustics array, consisting of two rows of ten sensors. The data, measured in the Alboran basin, late afternoon in midwinter between deep sea state condition 1 and 2, contained a strong controlled acoustic source, emitting a

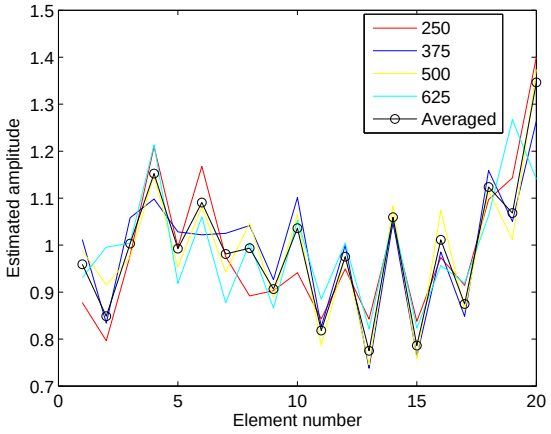

Fig. 7. ASV amplitude estimates.

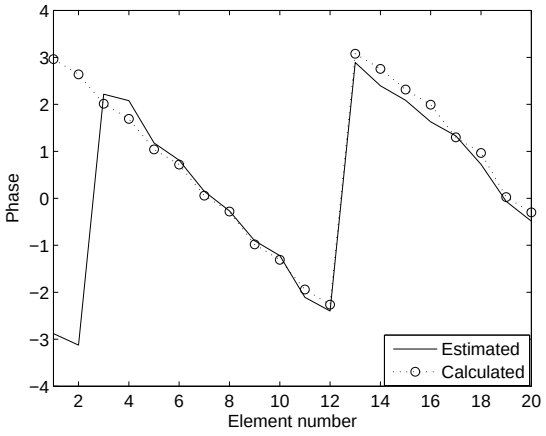

Fig. 8. A comparison of the estimated and calculated ASV phases.

tonal signal, which was towed behind another vessel in the far-field of the array. The time-series data were 50% overlapped, Hann shaded, and Fourier transformed to a resolution chosen to satisfy the bandwidth limit $B < 1/8T_{\text{transit}}$, where T_{transit} denotes the transit time across the array (see, e.g., [21]). Actual parameter values, e.g., frequencies, are proprietary and are therefore omitted. Here, only results from the frequency bin containing the tonal signal are examined. Part of the data was used to obtain calibration measurements, by using the spherical RCB (with a large radius) to estimate the true ASV. Figure 7 shows the gain estimates, measured at different times as well as the average gain, indicating that the measured gains do differ (significantly) from the assumed values of 1. Figure 8 compares the estimated and calculated[5] phases, indicating that there is a good match. To improve beamformer performance, one alternative is to apply a gain calibration to the data, before processing, and then allow for small variations in the uncertainty sets. However, these calibration measurements were obtained only for a single frequency and only from a subset of all possible AOAs. Therefore, a more sensible approach is to

[5]It is worth noting that the calculated phases are obtained for a source at the beam center and, therefore, the (slight) systematic error observed is due to the source not being precisely at the beam center.

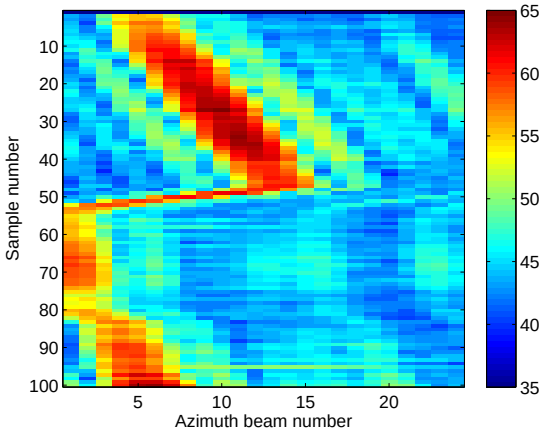

Fig. 9. Azimuth spectra, at one elevation, for the DAS beamformer.

instead use these calibration measurements to get an indication of the variations from the ideal case. Specifically, the radius of the uncertainty sphere used to allow for the gain calibration error has been estimated as[6] $\epsilon_{\text{gain}} = \sup_k \|\mathbf{1}_M - |\hat{\mathbf{a}}_k|\|_2^2$, where $|\hat{\mathbf{a}}_k|$ are the magnitudes of the kth estimated ASV, which from the results shown in Figure 7 gives $\epsilon_{\text{gain}} \approx 0.5$. We proceed to compare the DAS and RCB exploiting Tight Spherical Middle, Flat MVE, Flat LR, ND MVE and ND LR uncertainty sets, where the ND uncertainty sets are formed using a spherical error ellipsoid with $\check{\epsilon} = 0.5$. To obtain a well conditioned array covariance matrix, a rule of thumb is that $K \geq 2M$ independent and identically distributed snapshots are required, where M denotes the number degrees of freedom (DOF) [29]. Here, $M = 20$ and obtaining $K \geq 40$ snapshots, where stationarity could reasonably be assumed, was feasible. For a single elevation, Figure 9 shows the azimuth spectra for the DAS beamformer. Figures 10 and 11 illustrate azimuth and elevation spectra at sample 27, where the signal was strongest, for all of the beamformers. The results using either Flat LR or Flat MV ellipsoids are very similar, both of which suffer from severe SOI cancellation when pointing towards the strong calibration source. Out of the RCBs, the noise floor is highest for the flat uncertainty sets. The proposed ND LR and ND MVE sets are able to make the flat uncertainty sets they are derived from robust to arbitrary errors, such as calibration errors. They also able to give tighter control of elevation uncertainty compared to the tight spherical set. We remark that if the calibration error was smaller, so we could have reduced the radius of the spherical error ellipsoid, the gain in elevation localization would have been greater.

VI. Conclusions

In this paper, we have described fast, automatic methods for obtaining ellipsoidal ASV uncertainty sets for multi-dimensional arrays. These ellipsoids allow for angle-of-arrival (AOA) uncertainty in both azimuth and elevation and also for other, non-AOA errors, such as calibration errors. We have

[6]Here, we have first screened the data for outliers and erroneous measurements, and then used the supremum to obtain the radius of the sphere required to ensure that all observed calibration errors are taken into account.

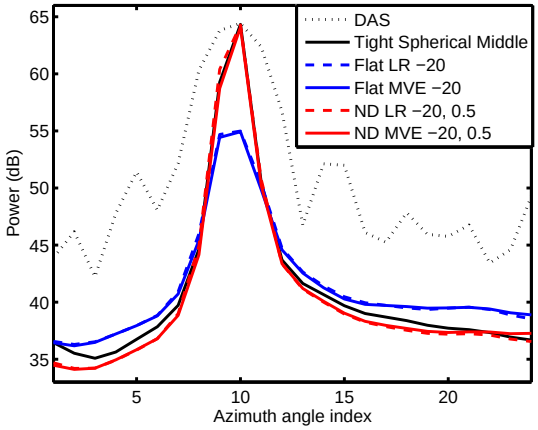

Fig. 10. Azimuth spectrum at elevation angle index 5, for sample 27.

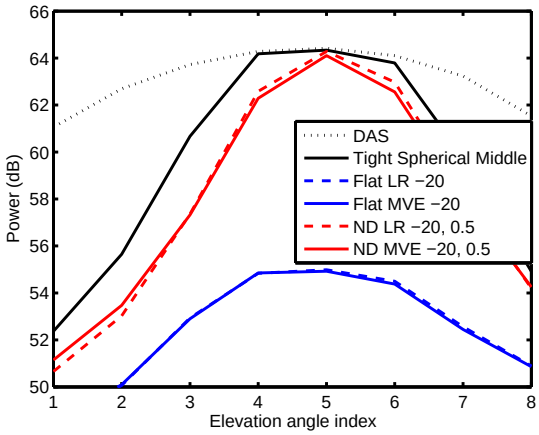

Fig. 11. Elevation spectrum at azimuth angle index 10, for sample 27.

modeled AOA uncertainty using flat ellipsoids and proposed fast, automatic methods for estimating them, including their dimension. The non-AOA errors are modeled using an *error ellipsoid*. We have proposed a simple computationally efficient technique for combining the AOA and error ellipsoids. Using both simulated data and data recorded from an underwater acoustics application, we have confirmed the benefits of exploiting the ellipsoids using recently proposed robust Capon beamforming techniques.

ACKNOWLEDGMENT

The authors would like to thank Dr Les Hart and Prof. Jian Li for their support and interesting discussions.

REFERENCES

[1] X. Guo, H. Sun, and T. S. Yeo, "Interference Cancellation for High-Frequency Surface Wave Radar," *IEEE Trans. Geoscience and Remote Sensing*, vol. 46, no. 7, pp. 1879–1891, Jul. 2008.

[2] Y. V. Shkvarko, "Unifying Experiment Design and Convex Regularization Techniques for Enhanced Imaging with Uncertain Remote Sensing Data-Part I: Theory," *IEEE Trans. Geoscience and Remote Sensing*, vol. 48, no. 1, pp. 82–95, Jan. 2010.

[3] S. D. Somasundaram, "Reduced Dimension Robust Capon Beamforming for Large Aperture Passive Sonar Arrays," *IET Radar, Sonar Navig.*, vol. 5, no. 7, pp. 707–715, Aug. 2011.

[4] P. Stoica and R. Moses, *Spectral Analysis of Signals*, Prentice Hall, Upper Saddle River, N.J., 2005.

[5] J. Capon, "High Resolution Frequency Wave Number Spectrum Analysis," *Proc. IEEE*, vol. 57, pp. 1408–1418, 1969.

[6] H. Cox, "Resolving power and sensitivity mismatch of optimum array processor," *Journal of the Acoustical Society of America*, vol. 54, no. 3, pp. 771–785, 1973.

[7] B. D. Carlson, "Covariance Matrix Estimation Errors and Diagonal Loading in Adaptive Arrays," *IEEE Trans. on Aerospace and Electronic Systems*, vol. 24, no. 4, pp. 397–401, July 1988.

[8] D. E. Grant, J. H. Gross, and M. Z. Lawrence, "Cross-Spectral Matrix Estimation Effects on Adaptive Beamforming," *J. Acoust. Soc. Amer.*, vol. 98, no. 1, pp. 517–524, July 1995.

[9] J. Yang and A. Swindlehurst, "The Effects of Array Calibration Errors on DF-Based Signal Copy Performance," *IEEE Trans. Signal Processing*, vol. 43, no. 11, pp. 2724–2732, November 1995.

[10] C. D. Richmond, "Response of Sample Covariance Based MVDR Beamformer to Imperfect Look and Inhomogeneities," *IEEE Signal Processing Letters*, vol. 5, no. 12, pp. 325–327, December 1998.

[11] D. Feldman and L. J. Griffiths, "A projection approach for robust adaptive beamforming," *IEEE Trans. Signal Processing*, vol. 42, no. 4, pp. 867–876, April 1994.

[12] H. L. Van Trees, *Detection, Estimation, and Modulation Theory, Part IV, Optimum Array Processing*, John Wiley and Sons, Inc., 2002.

[13] P. Stoica and J. Li, *Robust adaptive beamforming*, John Wiley & Sons, 2005.

[14] S. A. Vorobyov, A. B. Gershman, and Z.-Q. Luo, "Robust Adaptive Beamforming Using Worst-Case Performance Optimization: A Solution to the Signal Mismatch Problem," *IEEE Trans. Signal Process.*, vol. 51, no. 2, pp. 313–324, February 2003.

[15] R. G. Lorenz and S. Boyd, "Robust Minimum Variance Beamforming," *IEEE Trans. Signal Processing*, vol. 53, no. 5, pp. 1684–1696, May 2005.

[16] P. Stoica, Z. Wang, and J. Li, "Robust Capon Beamforming," *IEEE Signal Processing Letters*, vol. 10, no. 6, pp. 172–175, June 2003.

[17] J. Li, P. Stoica, and Z. Wang, "On Robust Capon Beamforming and Diagonal Loading," *IEEE Trans. Signal Processing*, vol. 51, no. 7, pp. 1702–1715, July 2003.

[18] J. Li, P. Stoica, and Z. Wang, "Doubly constrained robust Capon beamformer," *IEEE Trans. Signal Processing*, vol. 52, no. 9, pp. 2407–2423, Sept. 2004.

[19] Z. Wang, J. Li, P. Stoica, T. Nishida, and M. Sheplak, "Constant-Beamwidth and Constant-Powerwidth Wideband Robust Capon Beamformers for Acoustic Imaging," *J. Acoust. Soc. Amer.*, vol. 116, no. 3, pp. 1621–1631, Sep. 2004.

[20] S. E. Nai, W. Ser, Z. L. Yu, and H. Chen, "Iterative robust minimum variance beamforming," *IEEE Trans. Signal Processing*, vol. 59, no. 4, pp. 1601–1611, April 2011.

[21] S. D. Somasundaram and N. H. Parsons, "Evaluation of Robust Capon Beamforming for Passive Sonar," *IEEE J. Ocean. Eng.*, vol. 36, no. 4, pp. 686–695, Oct. 2011.

[22] P. Sun and R. M. Freund, "Computation of Minimum-Volume Covering Ellipsoids," *Operations Research*, vol. 52, no. 5, pp. 690–706, Sept.-Oct. 2004.

[23] S. D. Somasundaram and N. H. Parsons, "Using Robust Capon Beamforming to Minimise the Impact of Angle of Arrival Errors in 2-D Arrays," in *IEEE Workshop on Statistical Signal Processing*, 2009.

[24] T. L. Marzetta, "A new Interpretation for Capon's Maximum Likelihood Method of Frequency-Wavenumber Spectrum Estimation," *IEEE Trans. ASSP*, vol. 31, pp. 445–449, April 1983.

[25] A. Beck and Y. C. Eldar, "Doubly Constrained Robust Capon Beamformer With Ellipsoidal Uncertainty Sets," *IEEE Trans. Signal Processing*, vol. 55, no. 2, pp. 753–758, Jan. 2007.

[26] L. G. Khachiyan, "Rounding of Polytopes in the Real Number Model of Computation," *Math. Oper. Res*, vol. 21, no. 2, pp. 307–320, May 1996.

[27] G. H. Golub and C. F. Van Loan, *Matrix Computations*, The John Hopkins University Press, 3^{rd} edition, 1996.

[28] A. Kurzhanski and I. Valyi, *Ellipsoidal Calculus for Estimation and Control*, Birkhauser, Boston, MA, 1997.

[29] I. S. Reed, J. D. Mallett, and L .E. Brennan, "Rapid Convergence Rate in Adaptive Arrays," *IEEE Trans. Aero. and Elec. Sys.*, vol. 10, pp. 853–862, November 1974.